1982ApJ...260..183S

THE ASTROPHYSICAL JOURNAL, 260:183–201, 1982 September 1

RADIATION-DRIVEN IMPLOSIONS IN MOLECULAR CLOUDS[1]

MAXWELL T. SANDFORD II AND RODNEY W. WHITAKER
Los Alamos National Laboratory of the University of California

AND

RICHARD I. KLEIN
Berkeley Department of Astronomy, University of California, and Lawrence Livermore National Laboratory
Received 1981 July 29; accepted 1982 March 18

ABSTRACT

We present two-dimensional radiation-hydrodynamic calculations of the interaction of ionization and shock fronts with a geometrical inhomogeneity in a molecular cloud. These regions consist of low density clumps of masses $\leq 2\ M_\odot$, for which self-gravity is negligible. The radiation transport is both angle and frequency dependent. Ionizing stellar radiation and density variations in molecular cloud models are shown to produce a convergent shock that creates mass concentrations with densities significantly above those expected from one-dimensional compressions. The masses and time scale for concentrations to increase depend on the geometry of the initial density variations and the intensity of ionizing stellar radiation. The radiation of OB stellar associations is shown to be effective in forming dense mass globules from preexisting low density inhomogeneities near the edges of H II regions. Our calculations suggest that the cloud *environment* surrounding the cluster may influence subsequent star formation within the cloud. We include an analytic treatment of isothermal interacting shocks. The possible relationship between the observed concentrations and ionization shock compression is discussed.

Subject headings: hydrodynamics — interstellar: molecules — nebulae: H II regions — shock waves — stars: formation

I. INTRODUCTION

The interaction of ionizing stellar radiation with neutral gas in molecular clouds has long been recognized as a source for the propagation of shocks into clouds (see Spitzer 1968 and McKee and Hollenbach 1980 for reviews). Ambartsumian (1958) noted the occurrence of stellar associations in dense interstellar clouds, and Elmegreen and Lada (1977, hereafter EL) considered the possibility of star formation stimulated by ionization and shock (I-S) fronts originating from the most recently formed O stars in a subgroup near the molecular cloud.

Study of the effects of I-S fronts on the neutral material in molecular clouds may require an understanding of how cloud geometry affects the dynamical evolution of an H II region. Observations of molecular cloud morphology reveal regions showing that nearly all clouds contain small-scale inhomogeneities and clumps (Larson 1981). Star formation may proceed in a series of sequential bursts in smooth regions, but clumpy regions may require some other means (Sargent 1979 in a study of the Perseus OB2 cloud; Ho *et al.* 1979 in NH_3 observations of the Orion molecular clouds). Norman and Silk (1980) present additional evidence for clumpy structure in molecular clouds by reviewing observations in CO, NH_3, H_2CO, HC_3N, and CS.

In the context of clumpy cloud morphologies, the flows that result from ionizing radiation incident on cloud boundaries of both positive (concave to the radiation source) and negative (convex to the source) curvature could be markedly different (Whitworth 1979) and have significant effect on the evolution of the cloud as well as on the development of star formation. Observations of variable cloud morphologies motivated our initial study of the two-dimensional radiation-hydrodynamic interaction of ionizing radiation with curved, dense molecular clouds (Klein, Sandford, and Whitaker 1980, hereafter KSW). Schwarz, McCray, and Stein (1972) suggested that in a cooling medium non-planar compressions could lead to large density enhancements. In our first paper we considered the effect of radiation from a single O9 star on a preexisting cloud clump. These calculations did not include molecular cooling, but uncovered the interesting phenomenon of radiation-driven implosion of the cloud clump. Density compressions significantly above that predicted on the basis of one-dimensional, adiabatic, strong shock theory were found. These results suggested that two-dimensional I-S front compression of density inhomogeneities may change the time scale for sequential star formation as discussed by EL. It can be shown (Woodward 1980) that the EL model predicts compressed layers that become gravitationally unstable at a time $t_* = (0.717/G\rho_0)^{1/2}$ which depends only on the initial cloud density, ρ_0. This relation is essentially a consequence of the one-dimensional nature of their model. Comparing t_* with the free-fall collapse time of an undisturbed gas

---

[1] Authorship rotated.

cloud, $t_{ff} = (3\pi/32G\rho_0)^{1/2}$, one finds $t_* = 1.56t_{ff}$. Thus, one-dimensional compression is a less rapid star formation mechanism than free-fall collapse. As Woodward (1980) notes, EL must support their cloud against free-fall collapse (by invoking magnetic fields) long enough for the compressed layer to become unstable. Two-dimensional compressions reduce the value of t_* and provide a more efficient star formation mechanism than considered by EL. This paper continues our investigation of two-dimensional I-S fronts and presents results including molecular cooling. The geometries considered here are shown in Figure 1.

The implicit equations of radiation-hydrodynamics have been previously applied to formation of I-S fronts in the treatment of Klein, Stein, and Kalkofen (1978, hereafter KSK) who consider one-dimensional coordinates and include a detailed analysis for the non–LTE hydrogen atom. Radiative precursors and their gas dynamic consequences are calculated by KSK. The method of KSK may be difficult to use for two-dimensional calculations in interstellar gas dynamics because it is computationally prohibitive to consider all physical processes in a fully implicit manner. A simple method for modeling I-front positions and calculating I-S gas dynamics is given by Bodenheimer, Tenorio-Tagle, and Yorke (1979, hereafter BTY) who consider two-dimensional cylindrical coordinates and assume an isothermal gas. The work of BTY shows that many gas dynamic effects can be calculated without including a detailed treatment of I-S front coupling, but, as we shall show, BTY's method omits details of radiative transfer that contribute significantly to gas dynamic evolution. An implicit, two-dimensional treatment of the radiation-hydrodynamics equations is given in Sandford and Anderson (1973, hereafter SA1) and in Sandford *et al.* (1975) who use their method to calculate the cooling of a hot bubble. The physical detail of KSK's treatment is lacking in the work of SA1, although they recognize and discuss the disparity in dynamic and atomic (radiative) time scales elaborated later by KSK. The work of BTY does not encounter this difficulty since it only models the I-front position. Tenorio-Tagle (1976, hereafter TT) performed one-dimensional I-S front calculations that defined the evolutionary sequence of the structure, incorporating an artificial viscosity in the shock. The I-S front is shown to evolve from a weak R- to a weak D-front with several intermediate configurations, and it is shown that pressure, density, and distance in one dimension scale with the ambient cloud density. No previous work has considered the interactions of gas, dust, and radiation in calculations of I-S front propagation into molecular clouds.

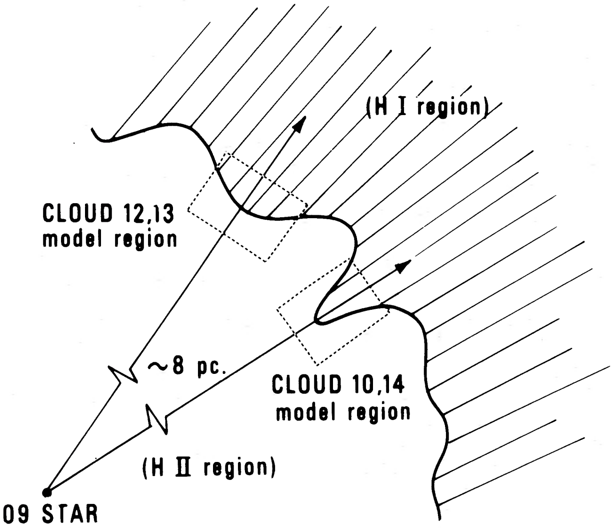

FIG. 1.—Schematic geometry for calculations. The direction from the O9 star is taken as the cylindrical symmetry axis for the computing grids (*dashed boxes*).

In this paper we consider the propagation of I-S fronts into uniformly dense clumps imbedded in molecular clouds of hydrogen gas. Our calculations are devoid of dust and magnetic fields, but we include molecular cooling. Two-phase (gas and dust) calculations will be addressed in future work. Radiation from a nearby (8 pc distant) O star is imposed as an isotropic intensity boundary condition. As before, density clumps are represented by considering a curved cloud geometry. We also consider a cloud having only slight curvature. The boundary radiation intensity is held constant for the duration (10^3–10^4 yr) of the calculations. Thus, stellar evolution of the ionizing star is not considered.

In § II we present the equations of radiation-hydrodynamics used in the present calculations as well as in our previous work. Equations given in our previous paper are erroneous. We include in § II approximations used and discuss the method of solution. In § III we give results of numerical calculations for models with initial computing cells of optical depth ≈ 1, and for optical depths $\gg 1$. We present an analytical analysis of the convergent shocks propagated by the I-front in § IV. In § V we discuss the possible role of I-S implosion in the formation of some observed objects, and in § VI we summarize our work.

II. EQUATIONS OF RADIATION-HYDRODYNAMICS

In the following subsections we give equations for two-phase flow radiation-hydrodynamics. Results presented in this paper do not include calculations with dust or self-gravity. We nevertheless give equations including two-phase flow because these terms illustrate the physical effects due to the second field (dust) that will be included in future work. The present computer code includes difference equations for all the terms that we give here. The nomenclature employed for variables is, in part, the following:

$\boldsymbol{u}_g$, $\boldsymbol{u}_d$ = velocity, with radial and axial components u and v in the cylindrical coordinate system, for gas and dust grains, respectively;

1982ApJ...260..183S

ρ_g = gas density, the actual microscopic mass density of gas as related to other thermodynamic variables by the equation of state;

ρ_d = dust density, the actual microscopic mass density of dust grains;

ρ_g', ρ_d' = macroscopic density, the mass of gas or dust per unit total volume;

p = total gas pressure, assumed to be locally in equilibrium between the two field components (gas and dust);

I_g, I_d = specific internal energy, related to temperature for the field components by an equation of state;

T_g, T_d = gas and dust grain temperatures;

θ = the volume per unit total volume available to the vapor, i.e., the fraction of volume that is occupied by vapor, known as the "void fraction";

Φ = mass fraction of gas that is dust vapor;

J_e, J_c = mass per unit time per unit volume evaporating or condensing and therefore interchanging between dust and gas fields;

K = drag function related to momentum exchange between fields;

R = exchange function describing the transfer of heat between fields;

ψ = specific energy of gravitational potential;

n_{H^0} = number density of neutral hydrogen;

n_{H^+} = number density of ionized hydrogen;

n_e = number density of electrons;

r_d = average radius of dust grains;

N = number density of dust grains;

X = fraction of hydrogen ionized;

I_ν = specific monochromatic intensity;

a_ν = hydrogen absorption coefficient;

σ_ν = dust opacity (cm^{-1});

$a_\nu{}^d$ = dust vapor absorption coefficient;

$\boldsymbol{\sigma}_{g,d}$ = viscous stress tensor for gas and dust.

a) *Hydrodynamics*

Our formulation builds upon the work of Harlow and Amsden (1975, hereafter HA) and Rivard and Torrey (1977, hereafter RT) for the Eulerian hydrodynamics equations. The interstellar medium is considered as composed of two "phases:" gas, which includes the ambient molecular and atomic species (H_2, H, H II in this paper), as well as a dust vapor component; and dust, which includes solid grains only. Two density variables are used for each phase and are distinguished by primed and unprimed symbols, which denote macroscopic and microscopic density values, respectively. The microscopic (unprimed) value is the thermodynamic density appearing in the equation of state for gas and is the material grain density for dust. The macroscopic densities (primed values) are those values actually present in a volume of the interstellar medium and are defined by introducing a connective variable θ known as the "void fraction." In addition, the number densities of neutral and ionic species are calculated as part of the equation of state and through rate equations.

Separate momentum equations allow the dust and gas phases to move independently because it is particularly important that future work properly treat the dynamical interaction of dust grains and gas. The mass fraction of dust is small, but the dynamical effects due to radiation pressure on dust grains may be significant.

The calculations in this paper do not include magnetic fields, dust, atomic species other than H, and cooling from molecules other than H_2. As consequence, the reader should note that for the purposes of this paper $\Phi = K = J_c = J_e = \rho_d' = 0$, $\theta = 1$, and $\rho_g' = \rho_g$ in the equations to follow. The effect of the present restrictions will be explored in future work.

Continuity equations for the gas and dust are

$$\frac{\partial \rho_g'}{\partial t} + \nabla \cdot (\rho_g' \mathbf{u}_g) = J_e - J_c \,, \tag{1}$$

$$\frac{\partial \rho_d'}{\partial t} + \nabla \cdot (\rho_d' \mathbf{u}_d) = J_c - J_e \,, \tag{2}$$

with the auxiliary equation for the dust vapor fraction:

$$\frac{\partial \Phi}{\partial t} + \nabla \cdot (\Phi \mathbf{u}_g) = \frac{\rho_g' + (J_e - J_c)}{\rho_g'} - 1 \,. \tag{3}$$

Momentum equations for the gas and dust fields are

$$\begin{aligned} \frac{\partial \rho_g' \mathbf{u}_g}{\partial t} &+ \nabla \cdot (\rho_g' \mathbf{u}_g \mathbf{u}_g) \\ &= -\theta \nabla p + K(\mathbf{u}_d - \mathbf{u}_g) \\ &\quad - \rho_g' \nabla \psi + J_e \mathbf{u}_d - J_c \mathbf{u}_g + \nabla \cdot (\theta \boldsymbol{\sigma}_g) \,, \end{aligned} \tag{4}$$

and

$$\begin{aligned} \frac{\partial \rho_d' \mathbf{u}_d}{\partial t} &+ \nabla \cdot (\rho_d' \mathbf{u}_d \mathbf{u}_d) \\ &= -(1 - \theta)\nabla p - (1 - \theta)\nabla p_r \\ &\quad - \rho_d' \nabla \psi + K(\mathbf{u}_g - \mathbf{u}_d) \\ &\quad + J_c \mathbf{u}_g - J_e \mathbf{u}_d + \nabla \cdot [(1 - \theta)\boldsymbol{\sigma}_d] \,, \end{aligned} \tag{5}$$

in which we assume that the diagonal components of radiation pressure p_r act only upon the dust component of the fluid. Neglect of radiation pressure for the gas component is justified by its small value when compared to the ion and electron gas pressure in the I-front. Although numerical diffusion greatly dominates real viscosity in our calculations, the Newtonian viscous stress tensors $\boldsymbol{\sigma}_g$, $\boldsymbol{\sigma}_d$ in equations (4) and (5) are included as given in RT, p. 4–5. The field momenta couple primarily through the drag exchange function. In the absence of evaporation or condensation, dust grains move with the gas unless radiation pressure drives the grain field sufficiently to transfer momentum to the gas Gilman (1972). Strong coupling can also occur in regions where phase transition occurs.

The energy equation for the dust phase is

$$\frac{\partial \rho_d' I_d}{\partial t} + \nabla \cdot (\rho_d' I_d \boldsymbol{u}_d)$$
$$= -p\left\{\frac{\partial}{\partial t}(1-\theta) + \nabla \cdot [(1-\theta)\boldsymbol{u}_d]\right\}$$
$$- (J_e - J_c)H_g + R(T_g - T_d) + (1-\theta)\boldsymbol{\sigma}_d : (\nabla \boldsymbol{u}_d)$$
$$+ \nabla \cdot [\kappa_d(1-\theta)\nabla T_d] + \int_0^\infty d\nu \int_0^{4\pi} d\Omega \sigma_\nu I_\nu$$
$$- 4\pi N r_d{}^2 Q_{\rm abs} \sigma T_d{}^4 , \qquad (6)$$

where H_g is the latent heat for phase transition and κ_d is the heat conduction coefficient for the solid material. The first term on the RHS of equation (6) accounts for work added to the gas field (subtracted from the dust energy density) due to the change in void fraction achieved by vaporizing or transporting dust. A similar term in the gas equation (7) cancels this term if dust and gas particles are dynamically "locked" with $\boldsymbol{u}_d = \boldsymbol{u}_g$ and phase change does not occur. The next terms account for energy density changes due to phase transition, interfacial heat conduction between fields, viscous stress, heat conduction within the dust field due to grain-grain collisional heating, grain heating by the absorption of ionizing radiation, and infrared emission by dust grains, where σ is the Stephan-Boltzmann constant, $Q_{\rm abs}$ is the infrared absorption efficiency factor for the dust, and N is the number density of grains. We assume the dust to be optically thin to infrared radiation. A diffusion approximation to the transfer of infrared radiation can be effected in equation (6) by appropriately defining κ_d.

The energy equation for the gas phase is

$$\frac{\partial \rho_g' I_g}{\partial t} + \nabla \cdot (\rho_g' I_g \boldsymbol{u}_g)$$
$$= -p\left[\frac{\partial \theta}{\partial t} + \nabla \cdot (\theta \boldsymbol{u}_g)\right] + \left[K + \frac{J_e - J_c}{2}\right](\boldsymbol{u}_g - \boldsymbol{u}_d)^2$$
$$+ (J_e - J_c)H_g + R(T_d - T_g) + \theta \boldsymbol{\sigma}_g : (\nabla \boldsymbol{u}_g)$$
$$+ \nabla \cdot \kappa_g \theta \nabla (T_g) - \lambda(T_g) n_{\rm H_2} \Gamma(X - 0.01)$$
$$+ n_{\rm H^0} \int_{\nu_0}^\infty d\mu \oint_0^{4\pi} I_\nu a_\nu d\Omega$$
$$- n_{\rm H^+} n_e \alpha(T_g)(kT_g + h\nu_0) , \qquad (7)$$

where $\alpha(T_g)$ is the recombination coefficient, k is Boltzmann's constant, $n_{\rm H_2}$ is the number density of molecular hydrogen, κ_g is the gas heat conduction coefficient, $\lambda(T_g)$ is the cooling rate for H_2 line emission (Gisler 1979), and $\Gamma(X - 0.01)$ is a cut-off function: equal 1 if the fraction of hydrogen ions <0.01, and 0 otherwise. The second term on the RHS incorporates the kinetic energy density imparted to the gas field by drag and phase changes. The last three terms incorporate effects of molecular cooling, ionization heating, and recombination cooling, respectively.

The gravitational potential specific energy ψ is found by solving Poisson's equation:

$$\nabla^2 \psi = 4\pi G(\rho_g' + \rho_d') . \qquad (8)$$

b) Radiative Transfer

The equation of radiative transfer is solved in cylindrical coordinates for a specified monochromatic, ionizing radiation flux incident on the lower boundary of the mesh and for a known intensity emitted by material in the cloud. The specific monochromatic intensity $I_\nu(r, z, t, \mu, \eta)$ includes the direct and diffuse radiation fields (Chandrasakhar 1960) and is defined at r, z, t by μ, the direction cosine to the cylindrical radius r, and η, the direction cosine of the angle taken from the positive z-direction (SA1). Since the velocity flows are small compared to the speed of light, the material is assumed to adjust instantaneously to the retardation effects of photon propagation, and thus we can write the time-independent equation of transfer as

$$\mu \frac{\partial I_\nu}{\partial r} + (1-\eta^2)^{1/2}(1-\mu^2)^{1/2}\frac{\partial I_\nu}{\partial z}$$
$$+ \frac{\eta^2(1-\mu^2)}{r}\frac{\partial I_\nu}{\partial \mu} + \frac{\mu\eta}{r}(1-\eta^2)\frac{\partial I_\nu}{\partial \eta}$$
$$= -\bar{a}_\nu I_\nu + j_\nu \rho_g' + \frac{\omega_0 \bar{a}_\nu}{4\pi}\oint_0^{4\pi} p(\boldsymbol{\Omega}, \boldsymbol{\Omega}') I_\nu(\boldsymbol{\Omega}') d\Omega' , \qquad (9)$$

where j_ν is the mass emission coefficient of the gas, ω_0 is the grain albedo, $p(\boldsymbol{\Omega}, \boldsymbol{\Omega}')$ is the normalized phase function for scattering by dust, $\bar{a}_\nu$ is the total opacity (cm^{-1}) defined by

$$\bar{a}_\nu = n_{\rm H^0}(1 - \Phi)a_\nu + \Phi \rho_g' a_\nu{}^d + \sigma_\nu . \qquad (10)$$

The mass emission coefficient is taken to represent the radiation of recombinations to the ground state of hydrogen. Thermal emission is not included since the amount of ionizing radiation from this source is small compared to the external stellar source. Equation (9) is solved subject to the lower boundary conditions

$$I_\nu(r, 0, t; \pm\mu, +\eta) = WB_\nu(T_*) , \qquad (11)$$

and

$$I_\nu(r, 0, t; \pm\mu, -\eta) = 0 , \qquad (12)$$

where W is the geometric dilution factor and T_* is the effective temperature of the ionizing star. At $r = R$ and $z = Z$ boundaries we take the inward intensities to be

$$I_\nu(R, z, t; -\mu, \pm\eta) = I_\nu(r, Z, t; \pm\mu, -\eta) = 0 . \qquad (13)$$

Solution of equation (9) subject to equations (11)–(13) gives I_ν at all r, z, at direction cosines μ, η, for time t.

c) Constitutive Equations

The equations of state for the gas are

$$p = \frac{\rho_g k T_g}{m_{\rm H} \bar{\mu}} , \qquad (14)$$

$$\theta = \frac{\rho_g{}'}{\rho_g} , \tag{15}$$

and

$$\rho_g I_g = \tfrac{3}{2}(n_{\mathrm{H}^0} + n_{\mathrm{H}^+} + n_e)kT_g + n_{\mathrm{H}^+} \chi_{\mathrm{H}} , \tag{16}$$

where χ_{H} is the hydrogen ionization energy and $\bar{\mu}$ is taken to be the mean molecular weight. The ionization rate equation (in Eulerian coordinates) is

$$\frac{\partial n_e}{\partial t} + \nabla \cdot (n_e \boldsymbol{u}_g) = n_{\mathrm{H}^0} \int_{\nu_0}^{\infty} d\nu \oint_0^{4\pi} I_\nu \frac{a_\nu}{h\nu} d\Omega - n_e n_{\mathrm{H}^+} \alpha(T_g) . \tag{17}$$

d) *Approximations to the Equations*

Equations for 12 field variables, $\rho_{g,d}{}'$, $\boldsymbol{u}_{g,d}$, Φ, $I_{g,d}$, ψ, I_ν, and $n_e = n_{\mathrm{H}^+}$, have been given. Our solution is made in cylindrical coordinates and does not provide separate continuity equations for the species particles; rather we calculate n_e from equation (17) and solve for neutral number density from

$$n_{\mathrm{H}^0} = \frac{\rho_g{}'}{m_{\mathrm{H}}} - n_e . \tag{18}$$

The details of molecular dissociation are not calculated, and it is assumed that molecular cooling is important only where the fraction of ionized hydrogen is less than $\sim 1\%$. The number density of hydrogen molecules effective in cooling the gas (n_{H_2} in eq. [7]) is estimated using dissociation coefficients from Aller (1963). Other molecules, especially CO, contribute to radiative cooling in the neutral cloud but are not included here. Our molecular cooling law $\lambda(T_g)$ removes energy from the gas for $T_g > 100$ K and results in the formation of isothermal shocks near this minimum temperature. A much more detailed treatment of the cloud molecular chemistry is impractical in these calculations.

The various quantities connecting the fields, such as J_e, J_c, K, R, κ_g, κ_d, are in general functions of the field and thermodynamic variables. In the results presented here we take $J_e = J_c = K = R = \kappa_d = 0$, initialize $\theta = 1$, $\rho_d = 0$ (pure hydrogen gas), and set $\kappa_g = 2.0 \times 10^{-4}$ ergs K^{-1} cm^{-1}. We have also approximated the recombination cooling coefficient, $\beta(T)$ (Spitzer 1978), as equal to the coefficient $\alpha(T_g)$. The kinematic viscosities needed to calculate $\boldsymbol{\sigma}_g$ and $\boldsymbol{\sigma}_d$ are taken as 1.0×10^{-3} (RT).

e) *Numerical Solution*

The equations for the 12 field variables are solved in cylindrical coordinates using a finite difference method. It is advantageous to solve the equations implicitly since phase transitions, which may occur on time scales short compared to that of the dynamics, are treated properly. Radiative processes can occur on a time scale short enough that the radiative transfer and rate equations must be solved implicitly (KSK). In our treatment it is found impractical to solve the radiation and rate equations implicitly with the hydrodynamics. The radiation and rate equations are solved explicitly at the beginning of each computational cycle. To achieve stability it is necessary to impose an additional time step criterion (SA1; KSK). This is accomplished by limiting the maximum relative change in both electron pressure and gas temperature to 0.15 per time step. The hydrodynamics equations (1)–(7) are advanced using the implicit, continuous, Eulerian (ICE) method (HA). The ICE method improves the time step when phase change occurs and when the flow is subsonic. For supersonic flow, the Courant condition can be violated only at the expense of accuracy. For problems in which the computing cells are $\gtrsim 1$ optical thickness, the explicit radiative method requires a smaller time step than allowed by the ICE method. The hydrodynamic difference equations actually used are extensive and readily available in RT; we therefore do not repeat them here.

Solution of the two-dimensional radiative transfer equation (9) has been studied extensively by those working in neutron transport theory. Two methods capable of including anisotropic scattering and solving I_ν directly are Monte Carlo (SA1) and the S_n (Lathrop and Brinkley 1973) finite difference method. Recent advances in two-dimensional radiative transport using Feautrier and Rybicki techniques hold great promise (Mihalas, Auer, and Mihalas 1978). To solve equation (9) the S_n technique is our method of choice. This method differences the transfer equation in space for each of $n(n+2)/8$ points in each quadrant in (η, μ)-space. We use the S_4 method which gives a total of 12 quadrature directions in angular dependence of I_ν. To include scattering, a higher order S_n may be required to resolve the angular dependence of I_ν that is introduced by the forward-throwing phase function of dust grains. Intensities are calculated by S_n from boundary and internal source values at every point r, z in the computing grid. The scattering integral is evaluated by iterative integration of the I_ν values.

Poisson's equation (8) for ψ is solved at each cycle using a difference method for solution of Hemholtz's equation (Adams, Swarztrauber, and Sweet 1979). The acceleration of gravity is held constant during the hydrodynamic iterations which is an acceptable procedure as long as accelerations due to self-gravity are not larger than those due to I-S fronts. Boundary conditions for Poisson's equation are Dirichlet-type, with the potential on the boundary calculated by an approximation to the far field:

$$\psi(r_i, z_j) = \sum_{k,l}{}' \frac{G m_{ij} m_{kl}}{(r_k{}^2 + z_l{}^2)^{1/2}} , \tag{19}$$

where i, j indicates a grid point on the boundary, G is the gravitation constant, the prime in summation indicates that $k, l \neq i, j$, and the sum is taken over the computing grid. The grid cell mass is defined by

$$m_{ij} = (\rho_g{}' + \rho_d{}')V_{ij} , \tag{20}$$

where V_{ij} is the volume of the grid cell.

III. CLOUD MODELS

This paper presents calculations on 25 × 50 and 80 × 50 uniform grids in cylindrical coordinates, with $\Delta r = \Delta z = 1 \times 10^{15}$ and 5.0×10^{16} cm. The bottom, right, and top of the grid are continuous hydrodynamic outflow boundaries. The right and top have zero albedo (outflow) radiation conditions. These calculations require extensive computer graphics to interpret results, although only limited examples can be given here. Radiation fluxes and gas velocities are plotted as vectors. Cell-centered variables are plotted as contours and also as surfaces viewed in perspective. On all vector and contour graphs the cylindrical symmetry axis is the left ordinate. In addition, we plot the individual variables T_g, ρ_g', p, and X along a cut parallel to the symmetry axis at a selected radial value. This graph facilitates interpretation of our results in one dimension. The nongray flux of ionizing stellar radiation is represented by blackbody radiation at $T_* = 30{,}000$ K, diluted to the value appropriate for an O9 star at 8 pc distance. The geometrical dilution factor is $W = 2.4 \times 10^{-15}$. Three frequency groups are used with $\nu = 3.290 \times 10^{15}$, 4.609×10^{15}, 5.934×10^{15} and $\Delta\nu = 1.325 \times 10^{15}$ Hz. This gives reasonable coverage in the Lyman continuum for this stellar temperature. Self-gravity is not significant for the masses computed in this paper, although the potential is calculated for display purposes.

The initial clouds have $n_{\text{H}^0} = 598$ cm^{-3}, $T_g = 15$ K, and are surrounded by fully ionized intercloud gas with $n_e = 0.24$ cm^{-3}, $T_g = 15{,}000$ K such that the two regions are approximately in pressure equilibrium. The results are not sensitive to the parameters chosen for the intercloud gas. Our smallest grid scale is chosen so that the optical thickness of a computing cell to ionizing radiation is ~0.5. The thickness of the I-front for 10 km s^{-1} velocity is $0.2/n_e$ pc, when n_e is taken in the I-front (Spitzer 1978) or approximately two cells in our calculation. The shock thickness (10^{11} cm) is considerably below the mesh resolution. We therefore expect the numerical results to correctly resolve the I-front and its coupling of energy to the S-front in our small-grid models. The S-front is not resolved.

Two geometries considered are shown in relation to the exciting star in Figure 1 and in Figure 2 which compares the initial ($t = 0$) density surfaces. The curved case is denoted Cloud 10 (25 × 50 grid) and represents the density inhomogeneities and clumps suggested by recent observations, although on a greatly reduced mass and geometric scale. The mass in Cloud 10 is 1.66×10^{-5} $M_\odot$. The more uniform model denoted Cloud 12 represents molecular clouds with spatially larger density variations.

The results of calculations for the Cloud 10 and Cloud 12 (80 × 50 grid) models are of interest because they resolve the I-front. One must also determine if the spatial scale of calculation can be increased to observed cloud masses without changing the phenomenology. Another calculation, similar to Cloud 10, was performed using a spatial scale 50 times larger. This calculation is identified as Cloud 14 (25 × 50 grid), and the initial molecular cloud contains ~2 $M_\odot$. The computing cells in Cloud 14 are optically thick, and therefore the I-front is not resolved. The stair steps in the initial density affect certain details of the dynamical evolution. As will be shown, the phenomenology of the Cloud 10 and Cloud 14 models is similar. We therefore conclude that although the details of the scaling procedure are not known, similar effects of I-S front compression should be observed throughout the mass range given here. Our discussion of cloud evolution is based upon the Cloud 10 and Cloud 12 models which resolve the I-S front structure, and conclusions are drawn from these and the more massive Cloud 14 case. To date, the small time steps required by molecular cooling have prevented calculations of very massive clouds.

a) *Radiation Flow*

The effect of cloud geometry on the flow of radiation is seen in Figure 3 which shows radiation flux vectors calculated in the first time step, when the intercloud medium is fully ionized and therefore relatively transparent to the ionizing radiation. Radiation is absorbed in the intercloud medium to maintain the ionization balance. The divergence of flux vectors at the right side of the computing mesh is a consequence of the open boundary condition (zero albedo). The vertical flux component is attenuated at the cloud edge due to absorption by the neutral gas. The radial component maximizes at the cloud edge in the outward (positive) radial direction. This effect is caused by a directional change of radiation at the cloud edge. The increased optical thickness at the cloud face causes some of the radiation to flow parallel to the face, preferring the direction where the photon mean free path is a maximum. Thus, it is necessary to solve the equation of transfer in a manner that preserves the directional properties of the flux integral.

A similar situation occurs in BTY's case 4 in which the stellar wind and radiation of an O star impinges upon a neutral globule. The BTY calculation shows a dynamical compression of the globule due to the stellar wind flow and the I-S front on the side facing the star, but their simplified one-dimensional treatment of the radiative transfer fails to reveal the significant dynamical effects that result from the radiation flow around the globule sides. BTY conclude that the globule must be close to its Jeans limit before compression occurs in order for star formation to follow. We show in the next section that I-S front implosion can produce density enhancements that might reduce the Jeans mass and decrease the time scale for star formation to occur. Therefore, a globule need not be close to its Jeans limit to eventually collapse.

b) *Cloud Dynamics*

Ionization at the cloud edge increases both temperature and particle density, enhancing pressure along the cloud edge. Partially ionized gas expands into the intercloud medium, and initially a weak R-type front moves

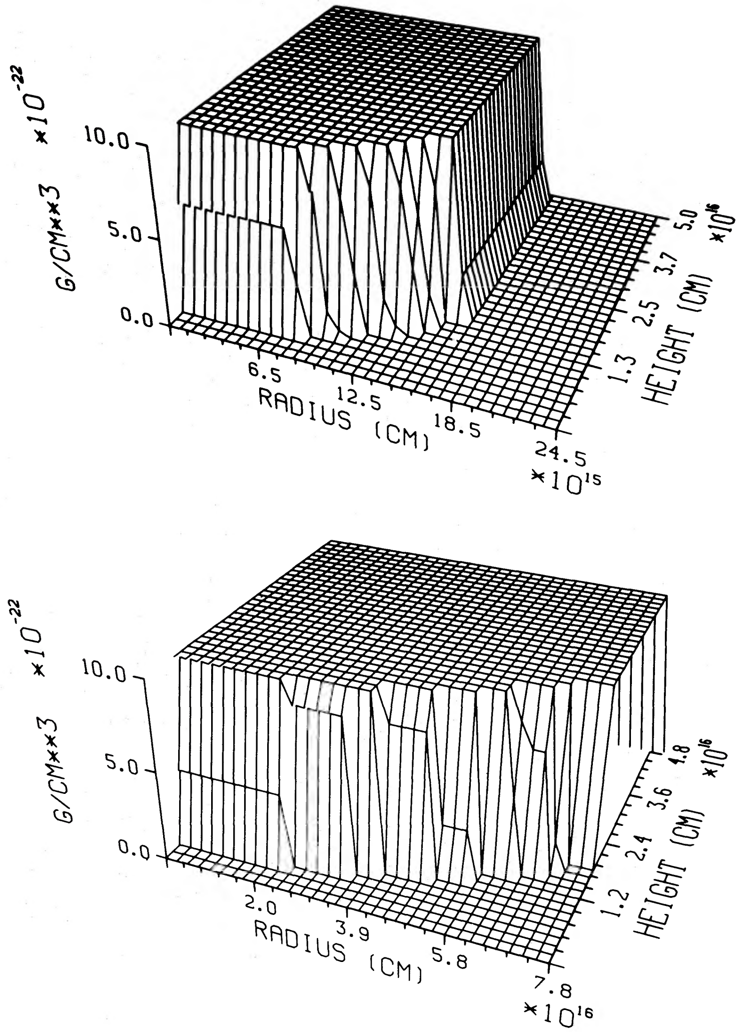

FIG. 2.—Initial ($t = 0$) density surfaces for molecular cloud models. The Cloud 10 model (*top*) represents a cloud with a curved density variation near the edge, and the Cloud 12 model (*bottom*) represents a smoother cloud.

into the cloud. In the case of the cloud of smaller radius (Cloud 10), the expanding gas diverges into the intercloud medium. The gas density is reduced, and the region remains relatively transparent to ionizing stellar radiation. On the other hand, the cloud of larger radius (Cloud 12) has gas outflow that is less divergent, and the gas passing through the I-front attenuates the stellar radiation to a greater degree (Spitzer 1978; Whitworth 1979). A portion of a clump with positive curvature would have convergent outflow. Such regions are clearly less transparent and thus absorb more radiation than the divergent gas flowing from clumps of negative curvature. Negatively curved regions will therefore have I-S fronts driven into them with greater strength than uniform or positively curved regions. Figure 4 shows velocity vectors at ~500 yr for the two cloud cases. The direction of velocity changes at the cloud boundary in both models, but the Cloud 10 case shows vectors within the cloud that converge from the sides of the cloud. At high z-values the interior velocities are mostly inward from the edge of the cloud in the Cloud 10 case. Gas flow in Cloud 12 shows little convergence inside the cloud, and the I-S front moves largely as in the one-dimensional analysis. The focused flow caused by the propagation of a two-dimensional shock is analogous to Woodward's (1976) calculation of the implosion of H I clouds due to passage of a spiral arm shock. A dense globule results from shock focusing, whether the source of the compressional energy be hydrodynamic, as in Woodward's work, or radiative in our results.

Neutral gas in the Cloud 10 case increases in density due to the converging flow field and isothermal compression. Figure 5 shows the mass concentration formed by this flow field, while Figure 6 shows the distribution of gas for Cloud 12. Comparison of Figures 5 and 6 shows that at comparable times compression in the curved model is greater and that a toroidal condensation is formed as a direct result of initial

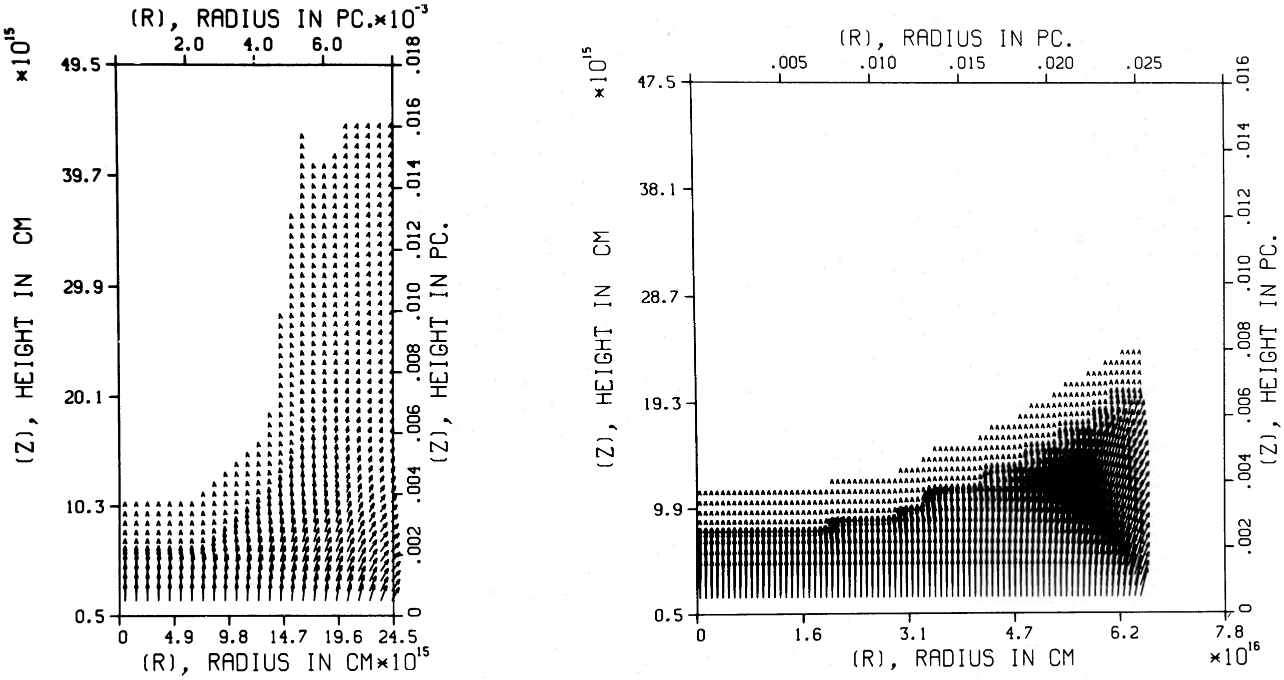

FIG. 3*a*

FIG. 3*b*

FIG. 3.—(*a*) Initial ($t = 0$) radiation flux vectors normalized to the maximum for the Cloud 10 model. Radiation frequency is in the Lyman continuum at $\nu = 5.934 \times 10^{15}$ Hz. (*b*) Initial ($t = 0$) radiation flux vectors for the Cloud 12 model. Normalization and frequency as in (*a*). Note that the radius and height plotting scales are chosen differently.

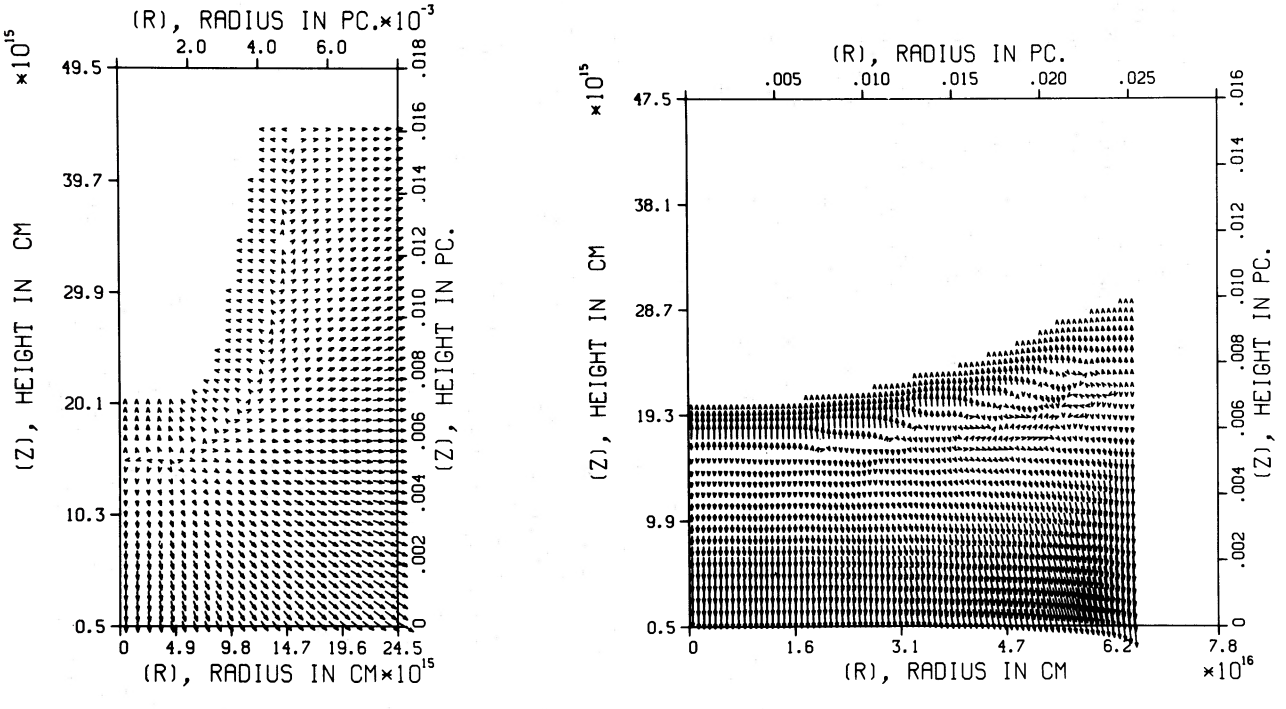

FIG. 4*a*

FIG. 4*b*

FIG. 4.—(*a*) Velocity vectors at $t = 1.61 \times 10^{10}$ s for the Cloud 10 model. Vectors are normalized to the maximum value of 32.9 km s^{-1}. (*b*) Velocity vectors at $t = 1.56 \times 10^{10}$ s for the Cloud 12 model. Vectors are normalized to the maximum value 19.0 km s^{-1}. Radius and height scales as in Fig. 3*b*.

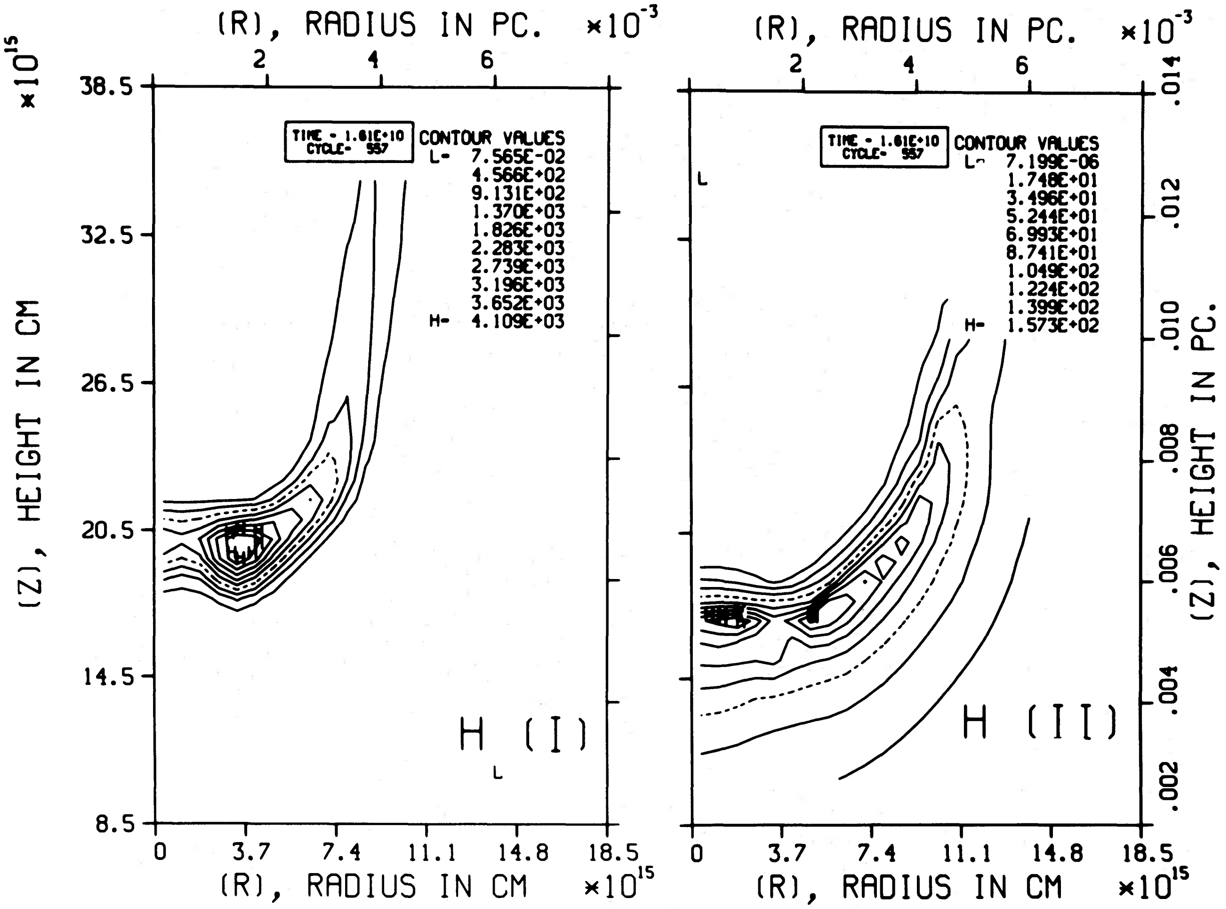

FIG. 5.—Density of neutral and ionized hydrogen (particles cm^{-3}) at $t = 1.61 \times 10^{10}$ s for the Cloud 10 model. The H II region surrounds the neutral condensation which is located near the cloud edge. High contour is marked by the letter *H*. Dashed contour is the fourth value above the lowest level.

cloud geometry and the basic axisymmetry of the problem. The two-dimensional I-front in the Cloud 10 model drives a curved shock into the cloud and compresses the neutral material by a factor of 7–8 at $t = 1.61 \times 10^{10}$ s.

The maximum compression in the Cloud 12 model at $t = 1.56 \times 10^{10}$ s (Fig. 6) is smaller than the Cloud 10 value by more than a factor of 2 because the I-S front is nearly planar and there is little shock focusing effect. The "staircase" density variations present in the initial conditions modify the evolution most in the Cloud 12 case. These variations act as sources for outflowing gas which, for the reasons discussed in § III*a*, are more effective in shielding the interface from ionizing flux in the Cloud 12 model. The harder Lyman continuum radiation penetrates the outflowing gas more effectively than it does near the ionization edge. The strength of the I-S front varies along the interface, and localized density compressions result (Fig. 6). These variations in the I-S front continue and grow with time. The maximum compression ratio in the Cloud 12 model is ~8 at $t = 4.95 \times 10^{10}$ s, suggesting a picture in which short-wavelength density variations along a cloud face may grow.

After 1300 yr of evolution, the Cloud 10 globule is driven toward the symmetry axis (Fig. 7). Once this occurs, the compression efficiency increases and the ratio reaches ~70. Figure 7 shows the H II region surrounding the neutral globule, and one would therefore expect this object to be observable in the radio continuum. The ionization is highest on the side of the globule facing the O star. Spherical or toroidal condensations are the only globule shapes possible in cylindrical geometry. If axial symmetry were not imposed, other centers of convergent flow could occur. Woodward (1976) also found that shock convergence drives the globule toward the symmetry axis. Ionization occurs around the edge of the neutral cloud, with the maximum at the cloud face presented to the illuminating star (Fig. 7).

A potentially important effect that has not been included in these calculations is the role of Lyα resonant scattering in affecting clump compression. For clouds that are optically thick to continuum radiation, each UV continuum photon produces a Lyα photon by

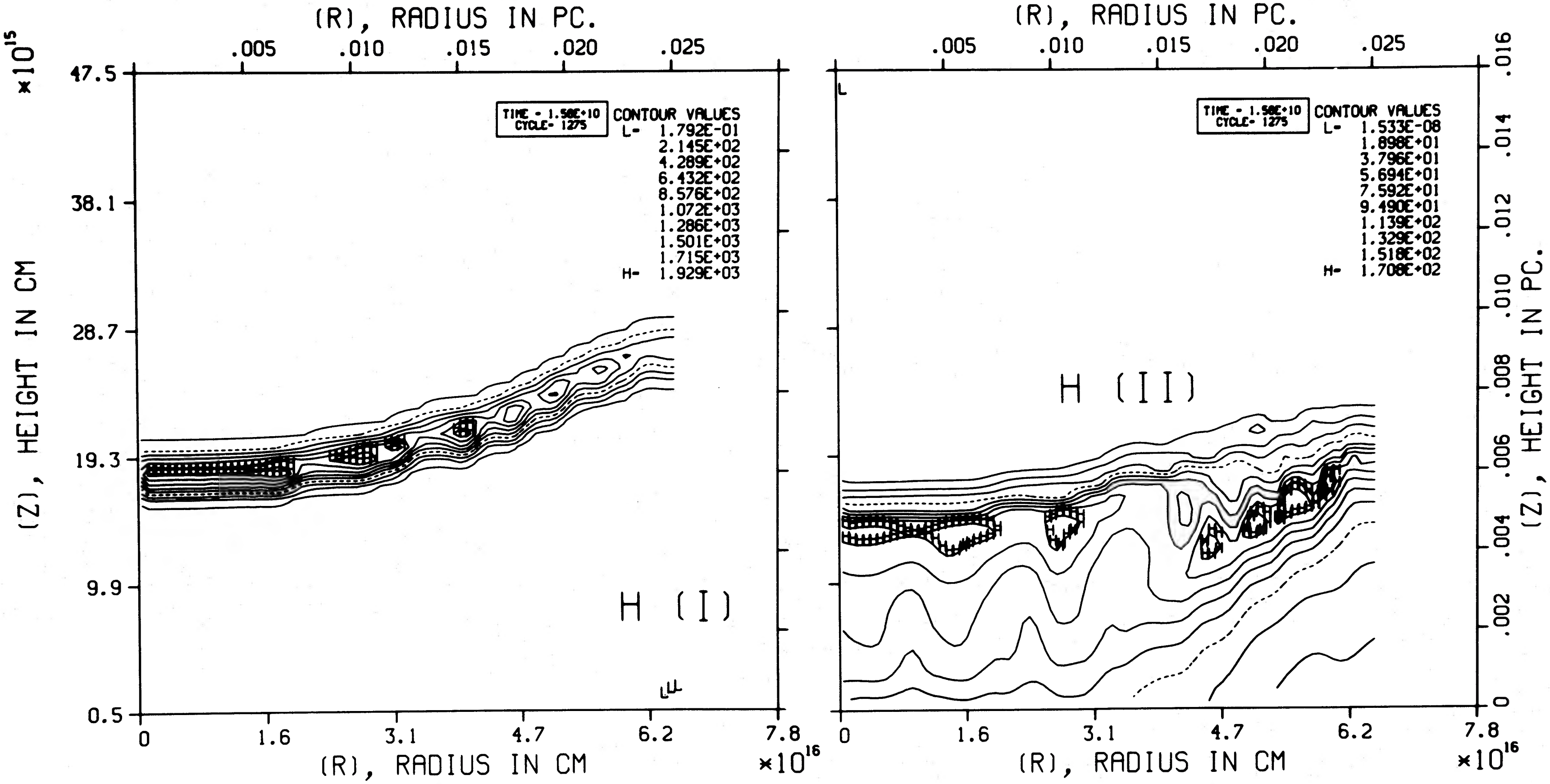

FIG. 6.—Density of neutral and ionized hydrogen (particles cm^{-3}) at $t = 1.56 \times 10^{10}$ s for the Cloud 12 model. The localized neutral concentrations along the cloud edge are much smaller than the concentration seen in Fig. 5. Contour levels are identified as in Fig. 5. Spatial scales are unequal, as in Fig. 3*b*.

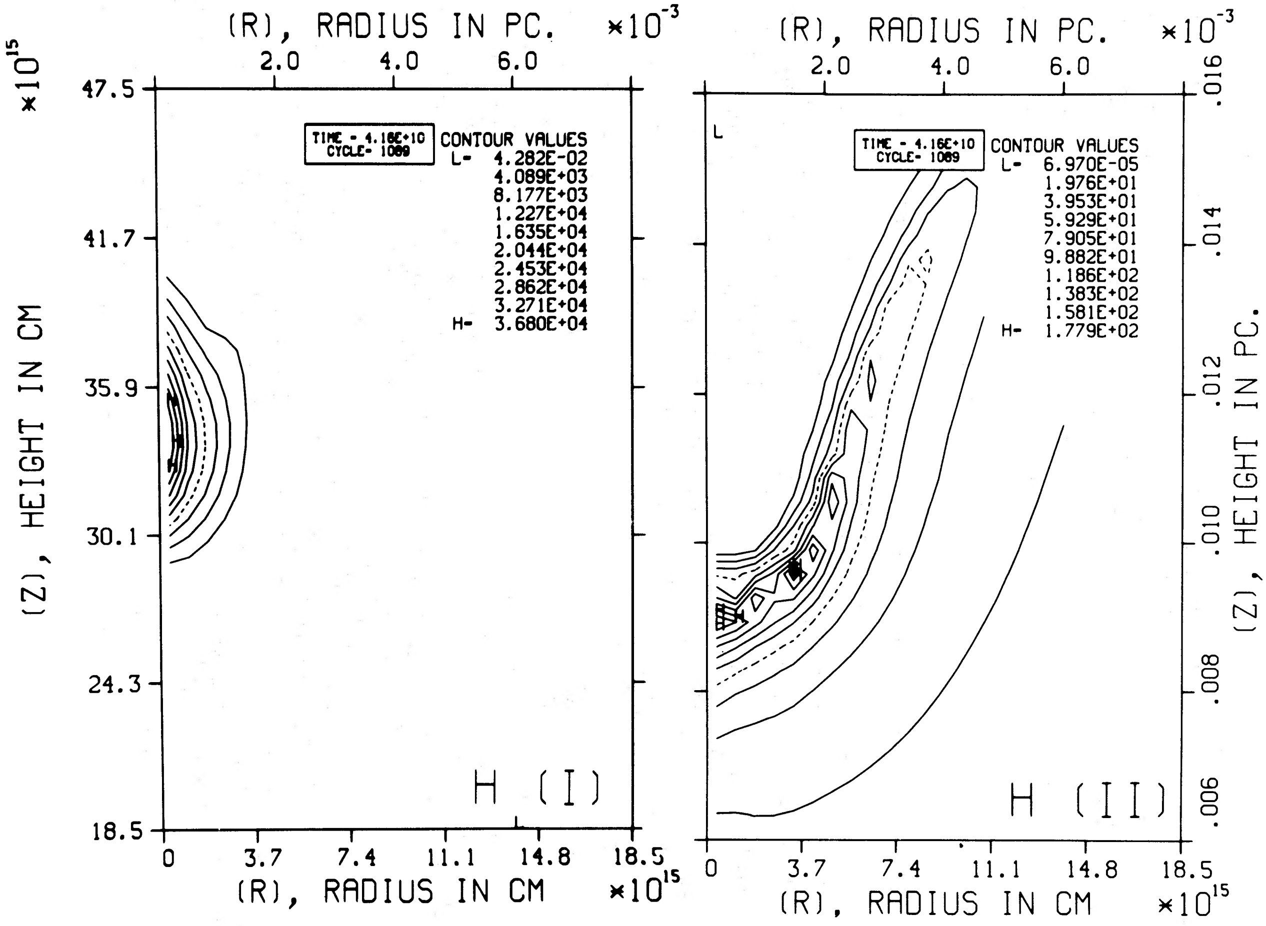

FIG. 7.—Density of neutral and ionized hydrogen (particles cm^{-3}) at $t = 4.16 \times 10^{10}$ s for the Cloud 10 model. Contour levels are identified as in Fig. 5.

recombination. Each Lyα photon has line center optical depth $\tau_e \approx (c/V_D)\tau_c$, where V_D is the velocity dispersion and τ_c is the continuum depth. Thus, substantial accelerations caused by the radiation pressure of multiply-scattered Lyα could reexpand and disrupt the clumps (Williams 1972; McKee and Tarter 1975). These disruptive effects would be offset by a reduction in the Lyα intensity due to expansion of the gas and by dust grain absorption. Nevertheless, Lyα radiation pressure is expected to mitigate the radiative implosions that we calculate.

c) *I-S Front Structure*

The I-front is initially of the weak R type and changes during the evolution of the cloud. Figure 8 presents one-dimensional plots of p, ρ_g', T_g, and X for the two models. Temperature in the I-front is affected by the balance of ionization heating, recombination cooling, and pdV work. The effect of heat conduction from the I-front into the neutral cloud is found to be negligible. In the S-front, viscous dissipation is balanced by molecular cooling.

The I-front at $t = 1.61 \times 10^{10}$ s in the Cloud 10 model is D type. It is preceded by a shock. The shocks are identified in Figure 8 by density peaks that occur in the toe of the I-front. The compression ratio in the Cloud 10 model is ~ 7 at $t = 1.61 \times 10^{10}$ s. The Cloud 12 structure is similar, but the compression ratio (2.7) is less, and the intercloud medium is generally cooler. The intercloud gas is cooler in the Cloud 12 model because, although the incident boundary flux is identical, the less divergent flow evaporated from the cloud results in denser gas that is more opaque, less highly ionized, and therefore is heated to lower specific energy. The one-dimensional structures are shown in Figure 9 for the Cloud 10 model later times.

The I-S structures shown in Figures 8 and 9 contain characteristic features that can be interpreted in terms of the physical processes occurring in the gas. Taking $t = 4.16 \times 10^{10}$ s (Fig. 9) as representative, one identifies the large density peak at $z = 3.5 \times 10^{16}$ cm as resulting from the isothermal compression of the convergent I-S front. The coincident pressure peak results from the equation of state. Moving to the left in the diagram, toward the radiation source one finds that temperature increases due to the destruction of molecules by radiation

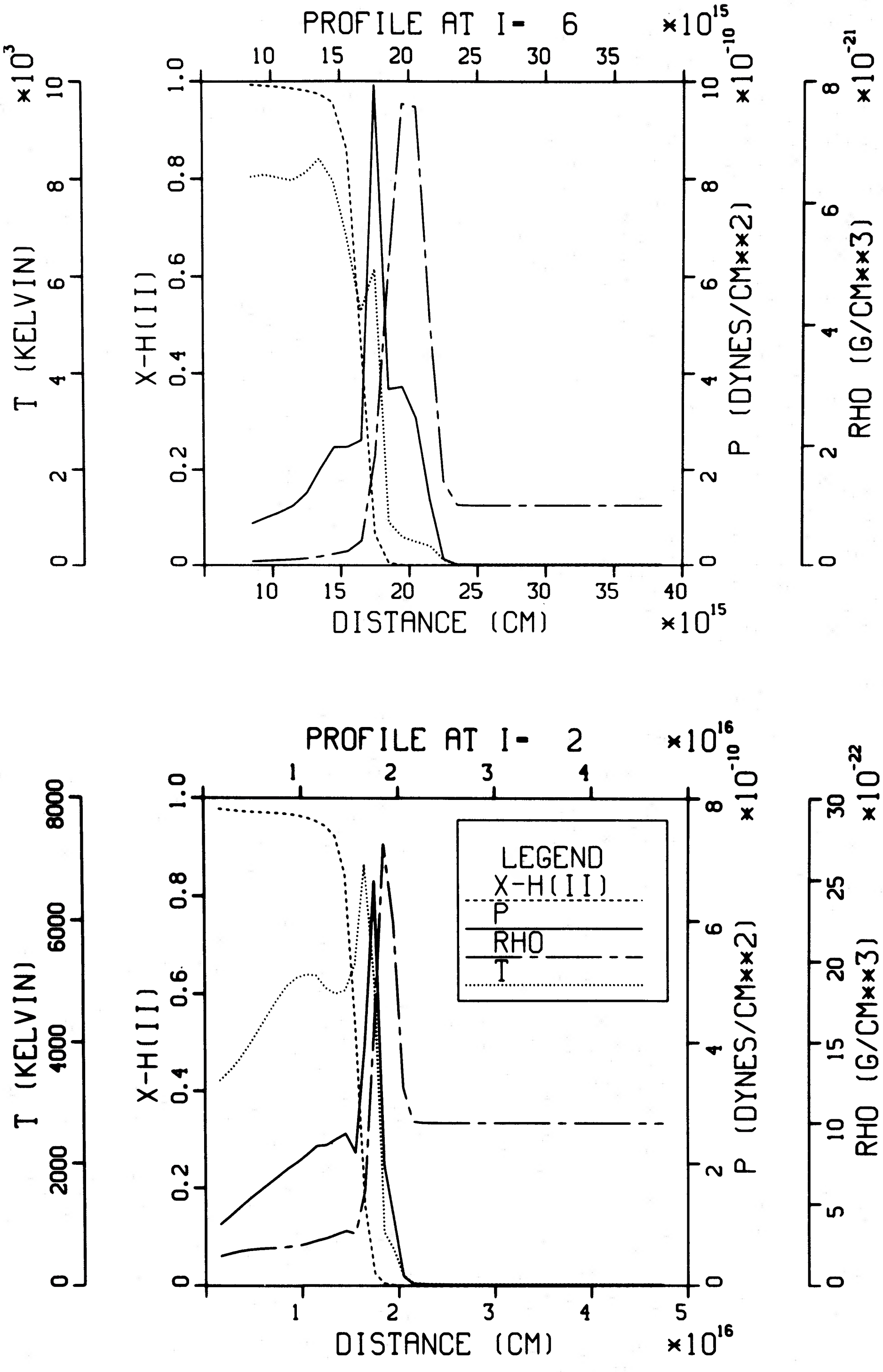

FIG. 8.—One-dimensional graphs of selected variables plotted vs. *z*-distance along a line parallel to the symmetry axis through the density maximum for Cloud 10 at $t = 1.61 \times 10^{10}$ s (*top*) and Cloud 12 at $t = 1.56 \times 10^{10}$ s (*bottom*).

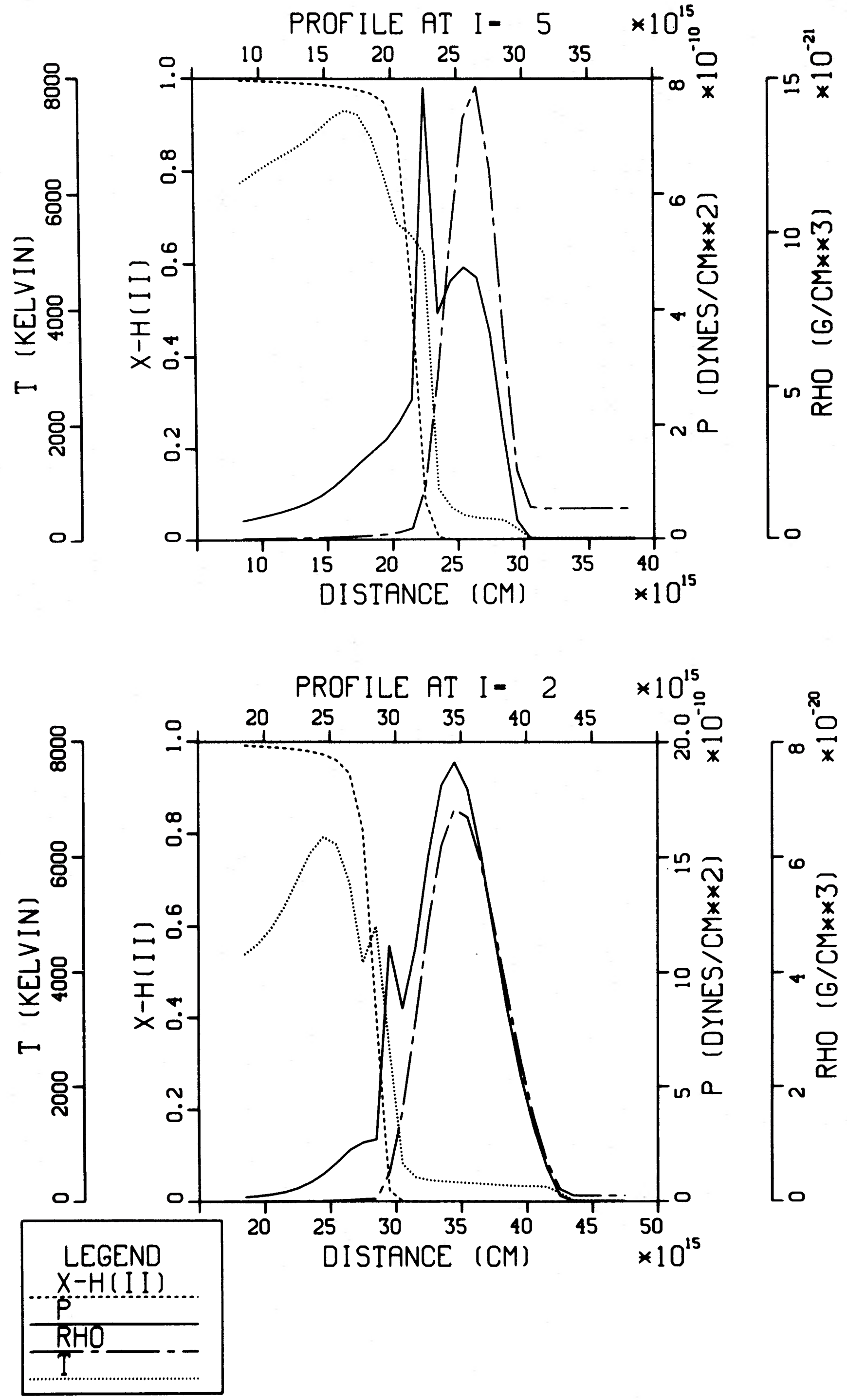

FIG. 9.—One-dimensional graphs of selected variables plotted vs. *z*-distance parallel to the symmetry axis for the Cloud 10 model at $t = 2.57 \times 10^{10}$ s (*top*) and $t = 4.16 \times 10^{10}$ s (*bottom*).

and the consequent loss of the cooling mechanism. The ion fraction and temperature both increase toward the left from $z = 3.0 \times 10^{16}$ cm due to the absorption of ionizing radiation. Pressure decreases from its compression peak at $z = 3.5 \times 10^{16}$ cm due to decreasing density, zero ionization fraction, and constant temperature, but it shows a second peak at the toe of the ion fraction curve due to the rapidly rising temperature. This thermal peak in pressure at $z = 2.9 \times 10^{16}$ cm constitutes the source for the accelerations that compress the neutral gas in the globule core. The peak marks the location of the S-front.

At $\sim$0.5 ion fraction, the temperature shows a dip. At the earlier time, $t = 2.57 \times 10^{10}$ s (Fig. 9, top), this appears as an inflection. This feature in temperature is coincident with the location of the maximum absorption of ionizing flux and the peak ion number density, and marks the location of the I-front.

The region to the left of the I-S front contains ionized gas moving away from the globule into the intercloud medium (Fig. 4*a*). The I-S front structure at this time is D type.

The separation of the I- and S-fronts in the Cloud 10 model is limited by convergence of the gas flow field. Figure 9 shows one-dimensional plots of the Cloud 10 variables at a time when the two-dimensional compression is well underway ($t = 2.57 \times 10^{10}$ s, $\rho/\rho_0 \approx 15$) and after the torus has collapsed to the axis ($t = 4.16 \times 10^{10}$ s, $\rho/\rho_0 \approx 68$). During the compression, the S-front pressure peak remains in the toe of the I-front, and the inflection in pressure that is coincident with the density peak in Figure 8 (top) grows, to become a broader, second peak.

For the Cloud 12 model, the pressure peak continues to separate from the I-front, and the compression ratio is $\sim$8 at $t = 4.95 \times 10^{10}$ s. Thus, compression in planar-type clouds is considerably less than in clouds with negative curvature because the amount of radiation absorbed at the cloud face is less and the planar cloud does not benefit by the additional compression that results from convergent flow.

We performed a calculation (Cloud 13) identical to Cloud 12, but using a radiation source 10 times as intense (10 stars at 8 pc distance). The I-S front in this model propagates as a weak R type. The effect of I-S compression for curved clouds driven by an R-type front has not yet been investigated.

We have investigated the I-S compression mechanism on a larger spatial scale in the Cloud 14 model with $\Delta r = \Delta z = 5.0 \times 10^{16}$ cm and otherwise identical properties to the Cloud 10 case. The evolution of this model is qualitatively similar to that of Cloud 10, except that the absorption of radiation at the cloud face near the axis is more advanced. A comparison of the internal energy, neutral hydrogen density, and velocity vectors for Cloud 14 in Figure 10 reveals that the toroidal condensation has an axial jet of ionized gas moving downward into the intercloud medium. Velocities near the axis reach 25 km s^{-1} at $z \approx 8 \times 10^{17}$ cm, and, as in Spitzer's (1978) discussion of the rocket effect, the material for this jet comes mostly from the neutral globule. The conical shape of the rocket cavity tends to collimate the velocity vectors. Acceleration for the jet material is provided by the hydrodynamic compression that raises the pressure in the cavity. The Cloud 14 one-dimensional plot at 1.88×10^{12} s is shown in Figure 11. The I-front preceeds an isothermal density condensation $\sim 2.5 \times 10^{17}$ cm thick. The mass in the condensation is $\sim 0.8\ M_{\odot}$, with an average density 8×10^{-21} g cm^{-3}. The compression ratio at this time is 19, corresponding to a neutral hydrogen density of 1.1×10^4 cm^{-3}. The average temperature in the globule is $\sim$100 K, and the mass is about two orders of magnitude from being Jeans unstable. It is likely that with further evolution and the addition of more molecular coolants the density will increase as the temperature decreases, and the globule may become Jeans unstable. The internal energy in the Cloud 14 model at $t = 1.88 \times 10^{12}$ s is $\sim 2 \times 10^9$ ergs g^{-1}, compared to the gravitational energy $\sim 5 \times 10^6$ ergs g^{-1}. The globule formed contains $\sim$40% of the initial cloud mass in both the Cloud 10 and Cloud 14 cases.

d) *Molecular Cooling Effects*

Comparison of the Cloud 10 model with our previous adiabatic results (KSW) reveals the effect of molecular cooling. Figure 12 shows one-dimensional plots of the adiabatic (Cloud 9) model, for which the peak density exceeds the strong shock limit due to the effects of flow convergence. In the Cloud 9 (adiabatic) model, pressure peaks slightly behind density in the shock. Temperature is highest in the ionized gas because of radiative heating, has a secondary peak in the I-front, and has an inflection due to viscous heating in the shock. In the cooled (Cloud 10, Fig. 9) model, temperature is nearly isothermal in the shock, and the peak density is larger than the Cloud 9 value. Molecular cooling is clearly an effect that must be considered in all future calculations, and it may be necessary to include additional molecules in our cooling model.

IV. CONVERGENT SHOCK WAVES

Our detailed two-dimensional calculations have shown that converging shocks produced by two-dimensional ionization fronts in molecular cloud inhomogeneities can result in larger density enhancements than produced by one-dimensional shocks. Two-dimensional calculations are presently computationally too expensive to allow the exploration of an extensive set of models. It thus becomes important to develop an analytical picture, both to realize an understanding of our numerical results, as well as to gain some insight into what the parameter dependencies of converging shocks are, and to set some upper limits as to the expected enhancements.

The numerical results indicate that significant density enhancements occur in a curved clump over those in a planar cloud before the shock converges to the symmetry axis. Once focused onto the axis of symmetry, the

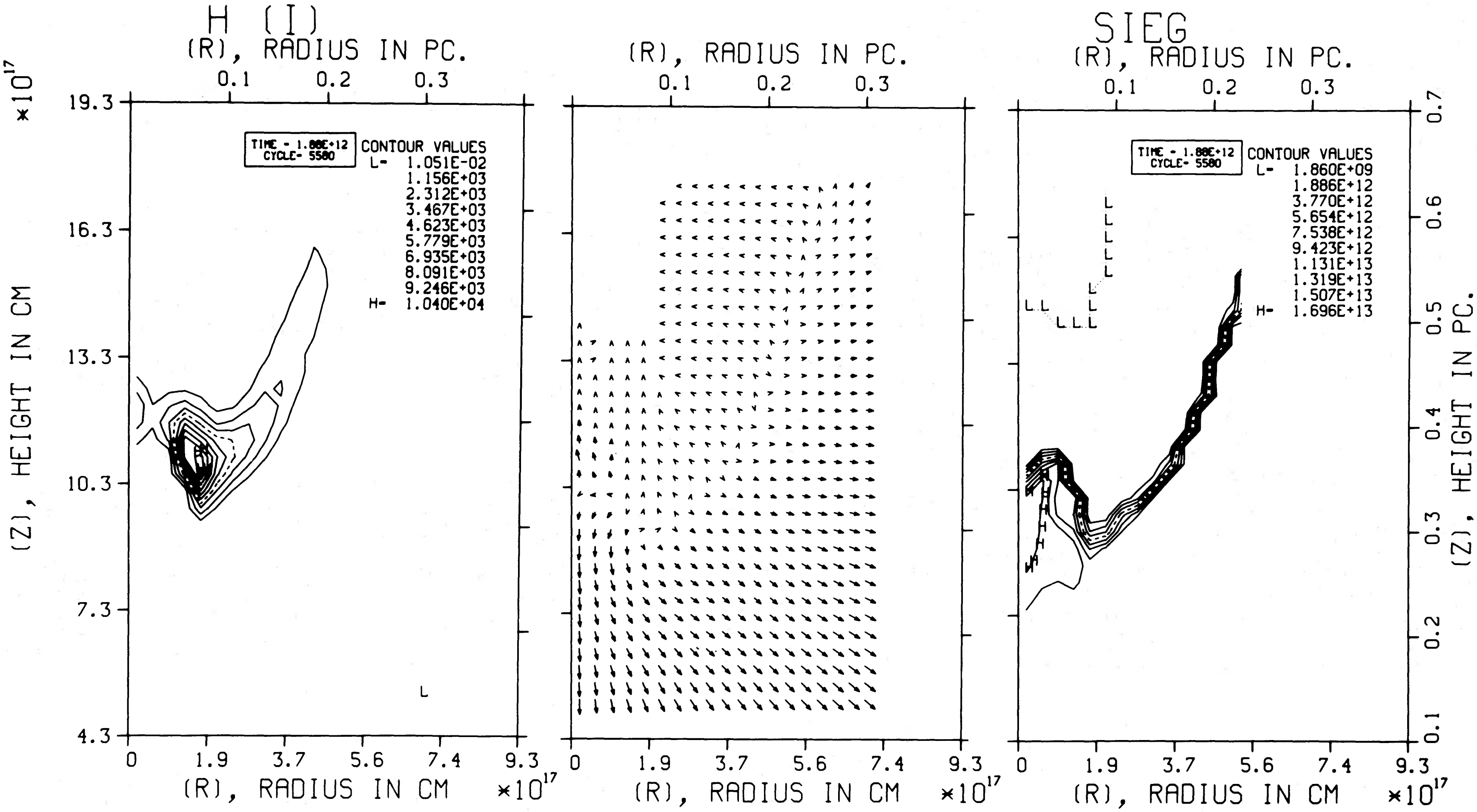

FIG. 10.—Contours of H I (particles cm^3), velocity vectors, and contours of specific internal energy (ergs g^{-1}) for the Cloud 14 case at 1.88×10^{12} s. Only a portion of the computing grid is shown.

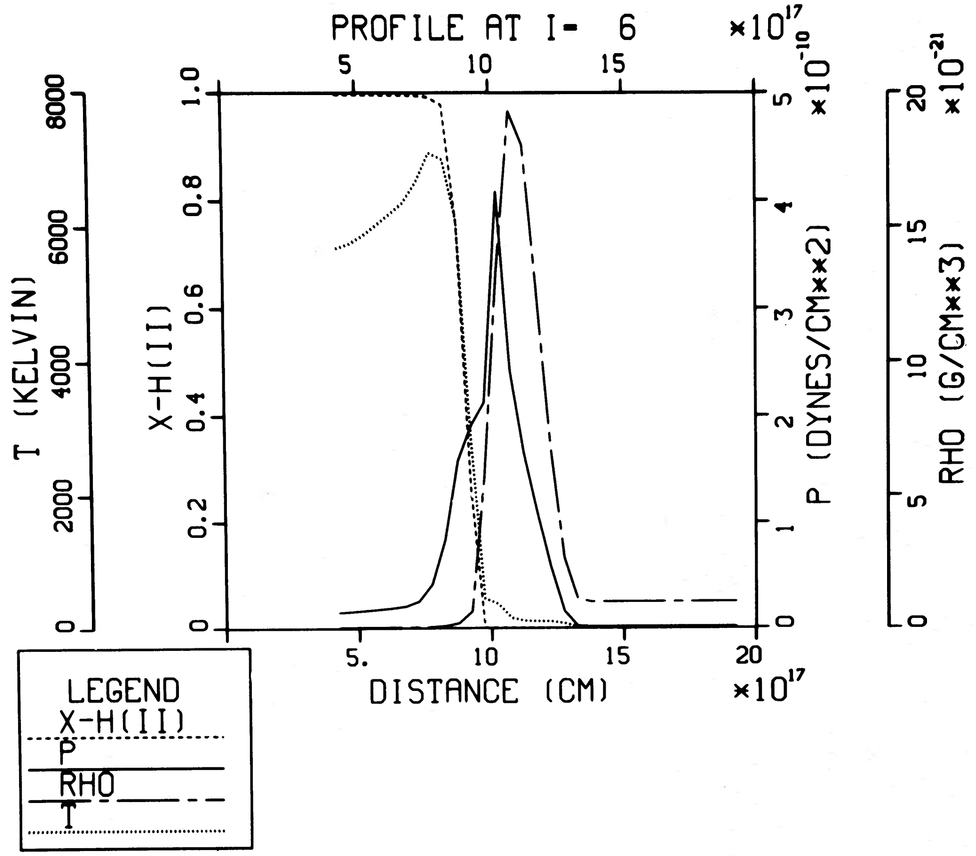

FIG. 11.—One-dimensional graphs of variables plotted vs. *z*-distance along a line parallel to the symmetry axis through the density maximum for Cloud 14 at 1.88×10^{12} s.

enhancement is even greater since the situation then represents a spherically convergent shock.

Let us consider the collision of two normal (head-on) colliding shocks for an adiabatic and also an isothermal gas. For shocks of equal strength we can consider the collision as the interaction of a single shock with a perfectly reflecting, rigid wall. We consider first the density enhancement after shock-shock collision in a gamma-law gas. Writing the shock adiabatic before and after collision and taking the strong shock limit, it can be shown

$$\frac{\rho}{\rho_0} = \frac{(\gamma-1)^2(\gamma+1)+(\gamma+1)^2(3\gamma-1)}{(\gamma-1)^2(\gamma+1)+(\gamma-1)^2(3\gamma-1)} . \tag{21}$$

For $\gamma = \frac{5}{3}$, we find $\rho/\rho_0 = 10$, which is a substantially larger compression than $\rho/\rho_0 = 4$, in the planar case. We note that equation (21) was derived with assumption of adiabatic conditions and does not apply for isothermal shocks ($\gamma = 1$).

The results of shock-shock collisions become far more impressive when we consider the *normal* collision of two isothermal shocks. This case is more representative of the physical situations we have calculated for molecular clouds but is clearly an upper limit since the numerical solution propagates shocks that intersect at an angle and are oblique to the flow through them. We apply the conservation equations of mass and momentum before and after collision (reflection) and make use of the isothermal equation of state $p = \rho C^2$, where C is the gas sound speed. Using the result that $\rho/\rho_0 = M_1{}^2$ before collision, where M_1 is the Mach number of each of the shocks before collision, we find that two solutions of a quadratic equation for $\rho_{\text{final}}/\rho_0$ are possible for reasonable choices of the sound speed. In the limit that $M_1{}^2 \gg 1$, a condition easily satisfied for the ionization front generated shocks, one of the solutions gives the identity result $\rho_{\text{final}}/\rho_0 = 1$. The other solution is $\rho_{\text{final}}/\rho_0 = M_1{}^4$. The compression thus obtained is substantially higher than a single planar shock, which produces a compression of $M_1{}^2$. For a radiatively driven implosion resulting from two-dimensional intersecting shocks, we can expect $M_1{}^4$ as an upper limit. For conditions prevalent in a neutral cloud, $M_1 \approx 10$ is not unreasonable, and compressions $\lesssim 10^4$ over the ambient density are possible. Density enhancements this high would have dramatic effects on lowering the Jeans mass, with reductions of $\sim 10^2$ possible. Thus, conditions for collapse to star formation could become very favorable.

1982ApJ...260..183S

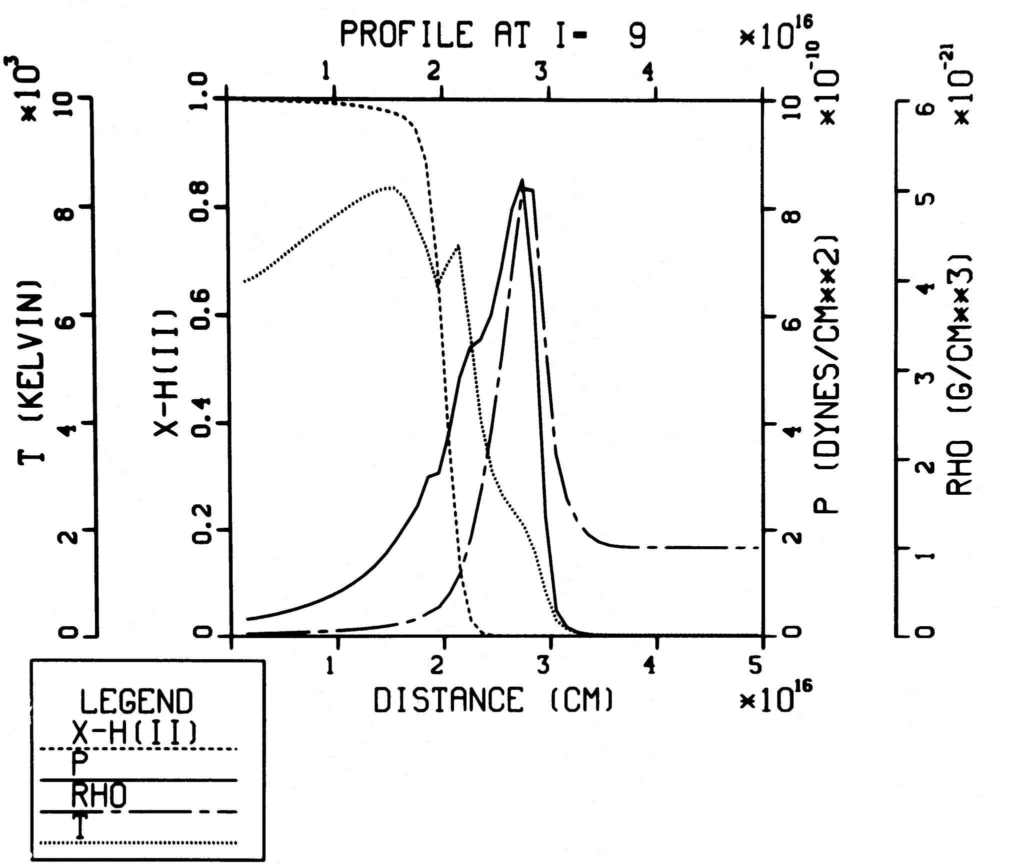

FIG. 12.—One-dimensional graphs of selected variables for the previously calculated (Cloud 9) adiabatic model at $t = 1.99 \times 10^{10}$ s

In order to gain an understanding of the magnitude of the density enhancements obtained in the two-dimensional calculations, it is necessary to consider the interaction of curved shocks. To a reasonable degree of approximation, it is possible to consider the intersecting curved shocks as an intersecting one-dimensional shock obliquely colliding at an angle ϕ with a reflected shock on the symmetry axis.

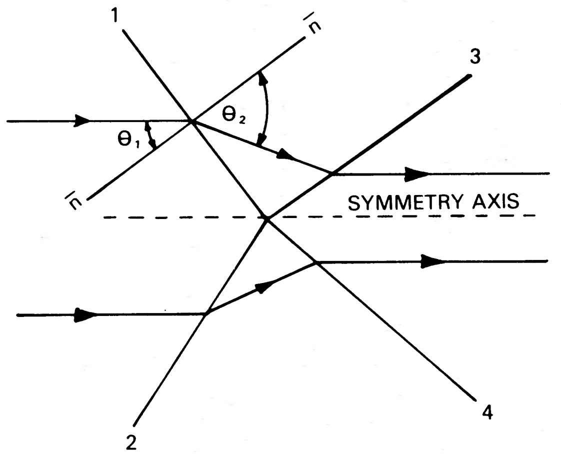

FIG. 13.—Schematic diagram of oblique shocks (1, 2) intersecting at the symmetry axis (*dashed line*) and resulting in two additional shocks (3, 4). Angle between the flow into the first shocks and the shock normal ($n - n$) is θ_1.

In steady state, we can represent the interaction schematically (Fig. 13) in the frame moving with the shocks, where θ_1 is the angle that the ambient fluid makes with the normal to the first shock and θ_2 is the angle the flow makes to the normal after passing through the shock. The first two intersecting shocks (1 and 2) will, within a select range of parameters, produce two further shocks (3 and 4), and thus the fluid gets shocked twice to its final compression on the symmetry axis. The angle θ_1 is related to the angle of separation of the shocks ϕ by $\theta_1 = (90 - \phi/2)$. Using the conservation of mass and the parallel and perpendicular components of the momentum conservation, it is possible to develop a cubic equation that relates the final compression ρ_3/ρ_1 to basic parameters M_1, the Mach number of the primary intersecting shocks, and θ_1 (Königl and Klein 1982). For simplicity it has been assumed that the intersecting shocks are symmetric and of equal strength. For the condition that $M_1{}^2 \sin^2 \theta_1 \gg 1$, they find that the cubic equation can be factored to a quadratic and yields two roots corresponding to shock compressions. For the two physical roots, they obtain

$$\frac{\rho_3}{\rho_1} = M_1{}^4 \sin^2 \theta_1 \cos^4 \theta_1 , \tag{22}$$

and

$$\frac{\rho_3}{\rho_1} = M_1{}^4 \sin^2 \theta_1 \cos^2 \theta_1 \ . \tag{23}$$

In choosing the prevailing solution, we refer to Henderson (1966) who points out that in the absence of strong disturbances in the downstream flow, the weaker solution, in this case equation (22), should dominate. We immediately note that in the collision of oblique shocks the very strong sensitivity to the Mach number $M_1{}^4$ is maintained; however, the upper limiting result of $M_1{}^4$ is now mitigated by the factor of $\sin^2 \theta_1 \cos^4 \theta_1$.

In our present numerical calculations, $M_{1,2} \approx 5$, and the angle of separation of the shock and its reflection is $\phi \approx 90°$, corresponding to $\theta_1 = 45°$. Thus, we find $\rho_3/\rho_1 \approx 78$. This is in excellent agreement with the Cloud 10 model which gives a density enhancement of 68 on the symmetry axis. It is clear that for initially stronger convergent shocks with similar separation angles, as could be produced by a source of several O stars, considerably higher compressions ($\rho_3/\rho_1 \approx 1250$ for $M = 10$) can be produced. Relatively large shock separation angles ($\phi \approx 90°$) are needed to produce the largest compressions. For clumps that are long and needle-like with small shock separation angle ($\phi \approx 30°$), the geometrical factor can reduce the effect of the $M_1{}^4$ compression considerably. Maximum compression for oblique shocks would occur at $\theta_1 = \tan^{-1}\left(\frac{1}{2}\right)$ corresponding to $\phi \approx 109°$. It is important that for angles such that $\sin^2 \theta_1 \cos^4 \theta_1 > 1/M_1{}^2$, the compression due to imploding clumps *dominates* the $M_1{}^2$ compression resulting for a planar one-dimensional compression from the usual picture of I-S propagation, and radiation-driven implosion thus becomes a more efficient way of producing Jeans unstable masses for star formation. For clumps that are not geometrically narrow, where convergent shocks are driven in at intersecting angles $\phi \approx 90°\text{–}120°$, and at relatively high Mach numbers, the compressions that result may greatly overwhelm the compressions possible with planar shocks. A limiting example of this is the implosion of a strong spherical shock wave in an adiabatic gas of uniform density. This problem was first addressed by Guderley (1942) and more recently by Zel'dovich and Raizer (1967). It is possible to obtain a limiting self-similar solution that applies in a region of small dimensions on the order of the radius of the front and close to the instant of collapse. The solution is not obtainable in closed form, but numerical solution of the resulting differential equations shows that the limiting density $\rho_{\text{final}} = 21.6\rho_0$ for a gas with $\gamma = \frac{7}{5}$, and this limiting density occurs somewhat *behind* the shock front because of the coalescence of many converging compression waves. After the instant of collapse, the shock wave reflected from the center propagates through the gas that is moving inward. Calculations show that the gas density behind the reflected shock is $\rho_{\text{ref}} = 137.5\rho_0$. This represents a substantial increase over the compressions achieved by a single adiabatic shock $\rho = 6\rho_0$ or the normal collision of two planar shocks $\rho = 21\rho_0$ for $\gamma = \frac{7}{5}$. For a spherically convergent isothermal shock, one can expect still greater compressions.

V. COMPARISON WITH OBSERVATION

In our first paper and in greater detail in the present work, we found that ionizing radiation from OB clusters interacts with small-scale geometric inhomogeneities in molecular clouds in a manner that causes a convergent flow and creates compressed regions. Inhomogeneities in clouds can be expected to form as a result of cloud cooling (Schwarz, McCray, and Stein 1972). The initial cloud variations are considered primordial, and we do not attempt to further explain their existence.

Recent observations by Ho *et al.* (1979) of the OMC-1 region and by Forster *et al.* (1981) of DR 21 reveal numerous globules of sizes 0.02–0.1 pc and density $n(\text{H}_2) \approx 10^5 \text{ cm}^{-3}$. These are too small to have been formed by gravitational collapse. The Cloud 10 model shows that I-S compression of low density clumps can result in small objects with densities $> 10^4 \text{ cm}^{-3}$. Our work suggests that such condensed objects may exist for a time near ionization fronts. The largest of these objects may become unstable to gravitational instability if one considers Hunter's (1979) modified Jeans criteria. The Jeans mass is reduced by factors of $\frac{1}{20}$ to $\frac{1}{5}$ in the presence of velocities $\sim 1 \text{ km s}^{-1}$ at 10 K.

Dibai (1958) first considered the compression of neutral globules in the vinicity of hot stars. Simple calculations led Dibai to conclude that several collisions between the ionization discontinuity and the surface of a globule could compress the globule sufficiently to shorten its gravitational contraction time. Until the work of KSW (1981) and the present paper, no detailed calculations of this process had been performed. The necessity of a more detailed treatment was recognized by Spitzer (1968, p. 26) in his review article. Israel (1980) demonstrated that in several of the fields observed, compact H II regions are found near the edge of compact CO clouds quite close to where a more expanded, less dense H II region touches the CO cloud. The inferred time and distance scales are too short and too small to apply EL's sequential star formation model. Israel hypothesizes that it is possible that the shock due to the expanding H II region triggers the collapse of a massive globule that was already present. Blitz and Thaddeus (1980) suggest similar phenomenology to explain their observations of the Rosette molecular cloud. It is possible that compact, dense globules could be formed from low density clumps by the radiation-induced coalescence discussed in this paper.

An object that may have formed as a result of I-S compression has been observed by Felli, Johnston, and Churchwell (1980). An unusual point source is found in the radio continuum in M17, near an arclike ridge of ionized gas. Felli *et al.* conclude that this object is probably a star of type B0 and that it may be an example of star formation induced by shock focusing.

VI. DISCUSSION

It is clear from recent observations that molecular clouds have inhomogeneous structure over a rather wide range of mass and spatial scales. The straightforward application of the I-S front interaction theory to relatively homogeneous clouds devoid of significant density or geometric variations can be expected to yield sequential star formation. However, it is significant that calculations which include the details of I-S front interactions in inhomogeneous regions produce small, dense condensations (globules) from larger, low density clumps. These *may* eventually collapse to form stars of relatively low mass. It must be kept in mind that we have not yet produced massive enough globules to calculate star formation. The calculations also indicate that an I-S front which moves into a geometrically inhomogeneous region may produce globules that will persist for some time but are *stable* to gravitational collapse. In either case, the sequential formation of OB stars is likely to terminate. Our calculations thus clarify the observational evidence that once a group of OB stars forms near a cloud, sequential star formation *does not necessarily follow* (Sargent 1979). This further suggests that the cloud environment surrounding the cluster influences subsequent star formation in the molecular cloud interior. The mass distribution of stars formed in a molecular cloud may depend upon the wavelength scale of the initial density perturbations in the cloud.

Our work has benefited by discussion with many people. MTS and RWW thank the previous (H. M. Agnew) and present (D. M. Kerr) directors of the Los Alamos National Laboratory for providing an environment in which this work could be done. RIK acknowledges the hospitality extended at Los Alamos by R. R. Brownlee and is grateful to B. Elmegreen, L. Blitz, P. Woodward, and A. Königl for many stimulating discussions. We would like to thank C. McKee and F. Harlow for a critical reading of the manuscript and an anonymous referee for helpful suggestions. H. Dickel provided preprints of observations of NGC 7538. This work was supported by the Los Alamos National Laboratory under USDOE contract W-7405-ENG. RIK acknowledges support from NSF AST 79-02866 and from the Lawrence Livermore National Laboratory.

REFERENCES

Adams, J., Swarztrauber, P., and Sweet, R. 1979, *FISHPAK: Fortran Subroutines for the Solution of Separable Elliptic Partial Differential Equations*, V. **2** (Boulder: NCAR).
Aller, L. H. 1963, in *The Atmospheres of the Sun and Stars* (New York: Ronald), p. 132.
Ambartsumian, V. A. 1958, in *Theoretical Astrophysics* (London: Pergamon), p. 516.
Blitz, L., and Thaddeus, P. 1980, *Ap. J.*, **241**, 676.
Bodenheimer, P., Tenorio-Tagle, G., and Yorke, H. W. 1979, *Ap. J.*, **233**, 85.
Chandrasekhar, S. 1960, *Radiative Transfer* (New York: Dover).
Dibai, E. A. 1958, *Soviet Astr.—AJ*, **2**, 429.
Elmegreen, B. G., and Lada, C. J. 1977, *Ap. J.*, **214**, 725.
Felli, M., Johnston, K. J., and Churchwell, E. 1980, *Ap. J.* (*Letters*), **242**, 157.
Forster, J. R., Goss, W. M., Wilson, J. L., Downes, D., and Dickel, H. R. 1980, *Astr. Ap.*, **84**, L1.
Gilman, R. C. 1972, *Ap. J.*, **178**, 423.
Gisler, G. 1979, private communication.
Guderley, G. 1942, *Luftfahrtforschung*, **19**, 302.
Harlow, F. H., and Amsden, A. A. 1975, *J. Comput. Phys.*, **17**, 19.
Henderson, L. F. 1966, *J. Fluid Mech.*, **26**, 607.
Ho, P. T. P., Barrett, A. H., Myers, P. C., Matsakis, D. N., Cheung, A. C., Chui, M. F., Townes, C. H., and Yngvesson, K. S. 1979, *M.N.R.A.S.*, **186**, 59.
Hunter, J. H. 1979, *Ap. J.*, **233**, 946.
Israel, F. P. 1980, *A.J.*, **85**, 1612.
Klein, R. I., Sandford, M. T., II, and Whitaker, R. W. 1980, *Space Sci. Rev.*, **27**, 275.
Klein, R. I., Stein, R. F., and Kalkofen, W. 1978, *Ap. J.*, **220**, 1024.
Königl, A., and Klein, R. I. 1982, in preparation.
Larson, R. B. 1981, *M.N.R.A.S.*, **194**, 809.
Lathrop, K. D., and Brinkley, F. W. 1973, Los Alamos Sci. Lab. Rept. LA-4848-MS.
McKee, C. F., and Hollenbach, D. J. 1980, *Ann. Rev. Astr. Ap.*, **18**, 219.
McKee, C. F., and Tarter, C. B. 1975, *Ap. J.*, **202**, 306.
Mihalas, D., Auer, L. H., and Mihalas, B. R. 1978, *Ap. J.*, **220**, 1001.
Norman, C., and Silk, J. 1980, *Ap. J.*, **238**, 158.
Rivard, W. C., and Torrey, M. D. 1977, Los Alamos Sci. Lab. Rept. LA-NUREG-6623.
Sandford, M. T., II, and Anderson, R. C. 1973, *J. Comput. Phys.*, **13**, 130.
Sandford, M. T., II, Anderson, R. C., Horak, H. G., and Kodis, J. W. 1975, *J. Comput. Phys.*, **19**, 280.
Sargent, A. I. 1979, *Ap. J.*, **233**, 163.
Schwarz, J., McCray, R., and Stein, R. F. 1972, *Ap. J.*, **175**, 673.
Spitzer, L. 1968, in *Stars and Stellar Systems*, Vol. **7**, *Nebulae and Interstellar Matter*, ed. B. M. Middlehurst and L. H. Aller (Chicago: University of Chicago Press), p. 1.
———. 1978, in *Physical Processes in the Interstellar Medium* (New York: Wiley), pp. 246–269.
Tenorio-Tagle, G. 1976, *Astr. Ap.*, **53**, 411.
Whitworth, A. 1979, *M.N.R.A.S.*, **186**, 59.
Williams, R. E. 1972, *Ap. J.*, **178**, 105.
Woodward, P. R. 1976, *Ap. J.*, **207**, 484.
———. 1980, *Early Solar System Processes and the Present Solar System*, LXXIII Corso Soc. Italiana di Fioica.
Zel'dovich, Ya, and Raizer, Yu. 1967, *Physics of Shock Waves and High Temperature Hydrodynamic Phenomena*, Vol. **2** (New York: Academic).

R. I. Klein: Lawrence Livermore Laboratory, A-Division, L-18, Livermore, CA 94550

M. T. Sandford II and R. W. Whitaker: Los Alamos Laboratory, Group ESS-5, MS-F665, Los Alamos, NM 87545